Hybrid Modulation Fault-Tolerant Control of Open-End Windings Linear Vernier Permanent-Magnet Motor With Floating Capacitor Inverter

Wenxiang Zhao, *Senior Member, IEEE*, Peng Zhao, Dezhi Xu, Zhonghua Chen, and Jihong Zhu

***Abstract*—In this paper, a new hybrid modulation fault-tolerant control of an open-end winding linear vernier permanent-magnet (OEW-LVPM) motor is proposed. By using a floating capacitor inverter, the proposed OEW-LVPM motor drive can continue operation under open-circuit fault condition. The OEW-LVPM motor fed by dual-inverter system consists of two inverters, which are connected to both ends of the motor windings, including a dc power named as main inverter (MI) and a floating capacitor called as capacitor inverter (CI). When one switch is broken in the CI, the CI topology will be restructured to a three-phase four-switch inverter. Then, an improved six-step modulation is investigated in the MI to reduce the switching frequency, while the conventional modulation is applied in the CI. Thus, the MI can provide all the active power, and the CI is only used to supply the reactive power. The proposed fault-tolerant control method is simulated and the experiments with the OEW-LVPM motor drive are also accomplished to verify the feasibility.**

***Index Terms*—Fault tolerance, floating capacitor inverter, hybrid modulation, inverters, linear motor, open-end windings (OEW), permanent-magnet (PM) motor.**

I. Introduction

NOWADAYS, linear motors have received increased attention in urban rail transit systems [1], [2]. Compared with the conventional transit systems based on the rotary motors, the urban rail transit systems employing linear motors eliminate costly and bulky rotary-to-linear transmissions. The linear motors in the direct-drive systems can be mainly classified into two

Manuscript received February 9, 2018; revised April 22, 2018; accepted May 21, 2018. Date of publication May 30, 2018; date of current version February 5, 2019. This work was supported in part by the National Natural Science Foundation of China under Grants 51777090 and 51422702, in part by the Research Fund for the 333 Project of Jiangsu Province under Grant BRA2017388, and in part by the Priority Academic Program Development of Jiangsu Higher Education Institutions. Recommended for publication by Associate Editor A. M. Trzynadlowski. *(Corresponding author: Jihong Zhu.)*

W. Zhao, P. Zhao, D. Xu, and Z. Chen are with the School of Electrical and Information Engineering and Jiangsu Key Laboratory of Drive and Intelligent Control for Electric Vehicle, Jiangsu University, Zhenjiang 212013, China (e-mail:

namely the common dc link, two isolated dc links, and a flying capacitor. When the dual inverter is fed by the common dc link, the zero-sequence current is expected to flow. An *et al.* [11]–[14] proposed several strategies to eliminate the zero-sequence current. To achieve the multilevel voltage waveforms and to cut the path of the common-mode current flow, two isolated dc sources are introduced into the traditional dual-inverter topology. In this topology, a four level is obtained when the OEW motor is fed by two separated inverters with unequal dc-link voltages, in which the ratio is 2:1 [15], [16]. This strategy achieves a better harmonic performance. For reducing the size and weight of the dual-inverter system with two isolated dc links, the dual inverter with a flying capacitor inverter was proposed. This topology has attracted much attention in the recent years. The one inverter connected dc source, called main inverter (MI), is controlled to provide active power, while the other inverter-connected flying capacitor, called capacitor inverter (CI), provides reactive power. Hong *et al.* [17] presented a charging method for the capacitor. In [18]–[20], to generate a multilevel output voltage, the particular voltage ratio of 1:0.5 or 1:0.366 was investigated, in which several modified modulation schemes were adopted to improve the waveform quality. In addition, it was used to extend the operation range [21]–[23].

On the other hand, the reliability of the motor drives is a key parameter in some critical applications and its improvement can be obtained by applying various methods. In the recent years, many fault-tolerant control strategies have been proposed to continue the operation of the faulty motor drive. The OEW motor fed by the dual-inverter system has additional degrees of freedom compared with the conventional single inverter. These degrees of freedom can be used for fault-tolerant operation when a part of the system fails. Nguyen *et al.* [24] investigated a fault-tolerant control strategy to remedy the short-circuit inverter fault for an OEW five-phase PM synchronous motor. However, no fault-tolerant control strategy was reported in dual inverter with a floating CI.

This paper will propose a novel hybrid modulation fault-tolerant control for an OEW-LVPM motor with a floating CI. There have been already many literature about fault diagnostic algorithms [25], [26]. The main topic of the proposed fault-tolerant control strategy is to remedy the switch open-circuit fault. When a switch is broken in the CI, the topology of the CI will be restructured to a three-phase four-switch inverter. Also, the improved six-step modulation is adopted in the MI, and the conventional modulation is adopted in the CI. Thus, the MI can provide all the active power, while the CI is only used to provide the reactive power for compensation. As a result, this OEW-LPMV motor can keep the same operating performance as prefault and the switching frequency of the inverter is also reduced. At the same time, the power factor of this system can be improved by using this control strategy. In Section II, the OEW-LVPM motor is analyzed and its mathematical model is established. The dual-inverter system with a floating CI and the relationship of power and voltage is also discussed. The hybrid modulation fault-tolerant control strategy is proposed in Section III. Moreover, in Sections IV and V, the performance of the proposed fault-tolerant control strategy is assessed by using the simulation and experiment results, respectively. Finally, the conclusions are drawn in Section VI.

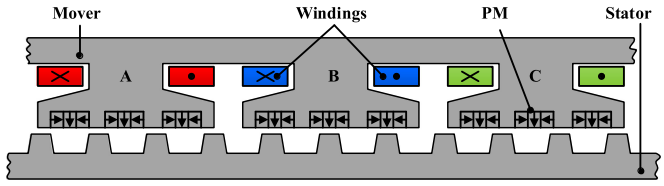

Fig. 1. Topology of an OEW-LVPM motor.

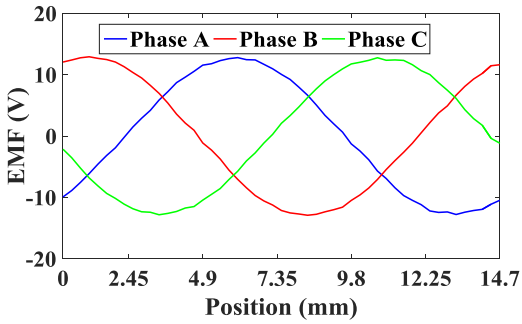

Fig. 2. Back EMFs at mover speed of 0.3 m/s.

II. OEW-LVPM Motor Drive

A. LVPM Motor

The topology of a three-phase OEW-LVPM motor is shown in Fig. 1. Its mover consists of the iron core with salient teeth, the armature windings, and a number of PM arrays which are mounted on the inner surface of the mover teeth, while the long stator is composed of the iron core only. The OEW-LVPM motor also adopts a special PM array. One PM array adopts three PMs, and the magnetization directions of these PMs differ from each other, as referred by the arrows in Fig. 1. The vertically magnetized PM is sandwiched between the two horizontally magnetized PMs, and the horizontally magnetized PMs reduce fringing leakage flux, hence improving air-gap flux density. The operation principle of this machine is based on the magnetic field modulation. The two-pole magnetic field produced by the three-phase armature windings on the mover is modulated by the stator teeth. This modulation produces nine-pole magnetic field in the air gap which interacts with the nine-consequent-pole PM field on the mover to produce thrust force. As a result, the OEW-LVPM motor has the advantages of high efficiency, high thrust density, and low cost, which is suitable for long stroke applications.

Figure 2 shows the back EMFs of this OEW-LVPM motor at the speed of 0.3 m/s. It can be seen that the back EMFs are very sinusoidal and symmetrical.

The motor model in the *d-q* coordinate system is also established. The voltage equation in the *d-q* coordinate can be

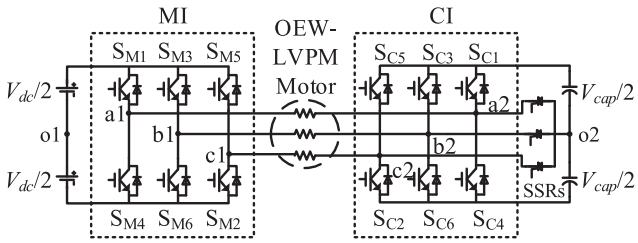

Fig. 3. Topology of dual inverter with floating CI.

expressed as

$$\begin{cases} U_d = pL_dI_d - \dfrac{2\pi v}{\tau}L_qI_q + R_sI_d \\ U_q = pL_qI_q - \dfrac{2\pi v}{\tau}(L_dI_d + \psi_{PM}) + R_sI_q \end{cases} \tag{1}$$

where I_d and I_q are the *d*-*q* axis currents, L_d and L_q are the *d*-*q* axis inductances, $\psi_{\rm PM}$ is the PM flux linkage, v is the mover speed, τ is the pole pitch, and $R_{\rm s}$ is the stator resistance. The p indicates differential operator (d/dt).

The thrust equation can be written as

$$F_e = \frac{3\pi}{\tau}[\psi_{\rm PM}I_q + I_dI_q(L_d - L_q)]. \tag{2}$$

B. Dual Inverter With Floating CI

Figure 3 shows the topology of the dual inverter with a floating CI. There are also three solid-state relays (SSRs) which can operate under faulty condition. The voltage vectors of the two inverters are defined by

$$\begin{cases} V_{\rm MI} = 2(U_{a1o1} + U_{b1o1}e^{j2\pi/3} + U_{c1o1}e^{j4\pi/3})/3 \\ V_{\rm CI} = 2(U_{a2o2} + U_{b2o2}e^{j2\pi/3} + U_{c2o2}e^{j4\pi/3})/3 \end{cases} \tag{3}$$

where U_{k1o1} and U_{k2o2} are pole voltages of the two inverters, respectively ($k = a, b, c$).

According to Fig. 3, the three-phase voltages of the motor are given as

$$\begin{cases} U_a = U_{a1a2} = U_{a1o1} - U_{a2o2} + U_{o1o2} \\ U_b = U_{b1b2} = U_{b1o1} - U_{b2o2} + U_{o1o2} \\ U_c = U_{c1c2} = U_{c1o1} - U_{c2o2} + U_{o1o2} \end{cases} \tag{4}$$

where U_{o1o2} is the voltage between the neutral point of MI and CI.

Based on (3) and (4), the voltage vector of the dual inverter can be obtained by subtracting $V_{\rm CI}$ from $V_{\rm MI}$

$$V_S = V_{\rm MI} - V_{\rm CI}. \tag{5}$$

For the single inverter, there are eight switching states and eight space voltage vectors, including six active vectors and two zero vectors. As to the MI, the eight vectors are denoted by 1–8, in which $1'$ to $8'$ are used to denote the eight vectors for the CI. Consequently, there are 64 possible combinations of the switching states for the dual inverter, and 19 different space voltage vectors, as shown in Fig. 4. They include 18 active vectors and one zero vector, the same as three-level inverters. The red circle indicates the maximum modulation range, and the length of the maximum voltage vector OG is $4U_{dc}/3$. Since the switching signals of two insulated-gate bipolar transistors (IGBTs) on the same leg are complementary, one signal can be used to get the ON-OFF state of each leg. For example, a combination $35'$ implies that the switching state for the MI is (0 1 0) and that for the CI is (0 0 1). A "1" indicates that a top switch in an inverter leg is turned ON and a "0" indicates that the bottom switch in an inverter leg is turned ON.

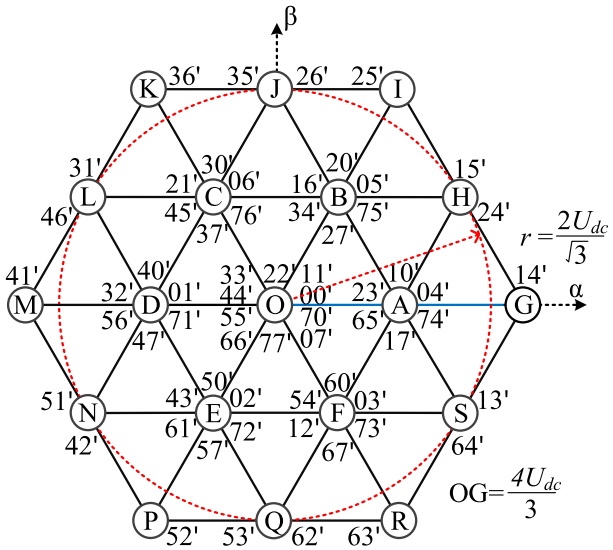

Fig. 4. Space voltage vectors of dual inverter.

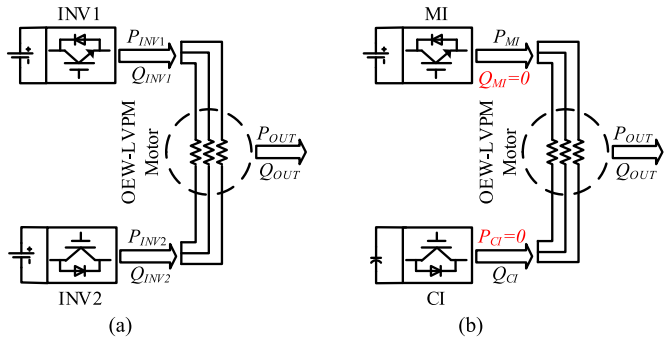

Fig. 5. Powers flow diagram. (a) Dual inverter with two isolated dc links. (b) Dual inverter with floating CI.

C. Power Regulation

The powers flow in the conventional dual inverter with two isolated dc links is shown in Fig. 5(a), where P and Q indicate the active and reactive powers, respectively, and the subscripts indicate the inverter, $P_{\rm INV1}$, $Q_{\rm INV1}$, $P_{\rm INV2}$, and $Q_{\rm INV2}$ indicate the input active and reactive powers to the motor, $P_{\rm OUT}$ and $Q_{\rm OUT}$ show the powers consumed by the motor. So, $P_{\rm OUT}$ and $Q_{\rm OUT}$ can be given as

$$\begin{cases} P_{\rm INV1} + P_{\rm INV2} = P_{\rm OUT} \\ Q_{\rm INV1} + Q_{\rm INV2} = Q_{\rm OUT}. \end{cases} \tag{6}$$

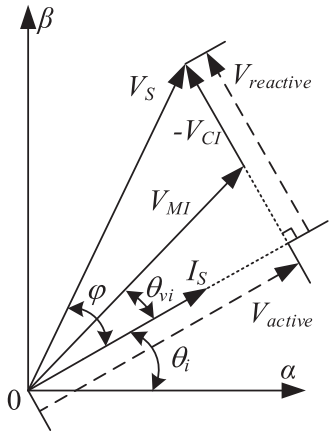

Fig. 6. Phase relationship between voltage vectors and current vector.

According to the previous analysis, the P_{OUT} and Q_{OUT} in the dual inverter with flying CI can also be expressed as

$$\begin{cases} P_{\mathrm{MI}} + P_{\mathrm{CI}} = P_{\mathrm{OUT}} \\ Q_{\mathrm{MI}} + Q_{\mathrm{CI}} = Q_{\mathrm{OUT}}. \end{cases} \tag{7}$$

Different from the control strategy of the conventional dual inverter with two isolated dc-links topology, the control strategy of the dual inverter with flying capacitor consists of two important parts, namely powers control and flying capacitor voltage control. To accomplish the first goal, the powers of this system are regulated. As shown in Fig. 5(b), in the conventional control method, the MI is controlled to only provide active powers P_{MI} and the CI is only used to provide the reactive powers Q_{CI} for compensation. It can be summarized as

$$\begin{cases} Q_{\mathrm{MI}} = 0 \\ P_{\mathrm{CI}} = 0. \end{cases} \tag{8}$$

From (7) and (8), P_{OUT} and Q_{OUT} in the dual inverter with a floating CI are regulated as

$$\begin{cases} P_{\mathrm{MI}} = P_{\mathrm{OUT}} \\ Q_{\mathrm{CI}} = Q_{\mathrm{OUT}}. \end{cases} \tag{9}$$

The currents flowing in the MI, CI, and the motor are identical under certain conditions. Thus, the output power depends on the phase angle of the output voltage vectors and the current vectors of each inverter. Fig. 6 shows the phase relationships between the reference voltage vector V_S and the current vectors I_S in the dual inverter with floating CI, V_{MI} and V_{CI} are the voltage vectors of the MI and the CI, respectively, V_{active} is the active component of the reference voltage vector, V_{reactive} is the reactive component of the reference voltage vector, θ_i is the angle of I_S, θ_{vi} is the angle between V_{MI} and I_S, and φ is the power factor angle. By controlling the output voltage vector of the MI in parallel with the current vector, Q_{MI} becomes zero. Also, P_{CI} becomes zero when the angle between the current vector and the output voltage vector of the CI is 90°. Thus, by applying the dual inverter with flying CI topology, the power factor of system can be increased. This effect is more obvious when the motor operates in the high-speed region or in high load region. As shown in Fig. 6, the angle φ is constant in a fix speed region, but the voltage vector V_S increases as the speed increases according to (1). The faster the motor runs, the higher voltage vector V_S is required and the higher reactive voltage is also increased. In summary, the dual inverter with a floating CI system lightens the burden of reactive power and improves the efficiency of the motor in the high-speed region.

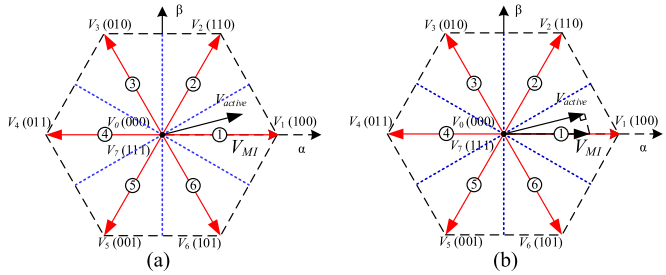

Fig. 7. Modulation of MI. (a) Conventional six-step modulation. (b) Improved six-step modulation.

III. Hybrid Modulation Fault-Tolerant Control Strategy

In this section, a hybrid modulation strategy for the OEW-LVPM motor with a floating CI will be proposed, in which an improved six-step modulation strategy is investigated in the MI. Besides, when one switch is broken in the CI, a fault-tolerant control strategy is deduced to keep the motor operation as prefault.

A. Improved Six-Step Modulation

At present, there are three representative modulation methods, namely sinusoidal pulsewidth modulation (PWM), space vector PWM, and six-step modulation. The maximum modulation indices of the sinusoidal PWM and the space vector PWM are 0.7854 and 0.9067, respectively. While the six-step modulation can provide the maximum modulation indices of 1. For the conventional motor drive employing a single inverter, by adopting the six-step modulation, it generates odd harmonics which will lower the efficiency and cause the torque ripple and noise. However, in the dual inverter with a floating CI topology, the voltage vector required by the motor is synthesized by the voltage vectors supplied by the dual inverter. The dual-inverter topology can solve these problems. Based on the compensation of the floating CI, the currents are maintained in very sinusoidal shape. In summary, the six-step modulation adopted in the dual inverter removes its disadvantages.

The improved six-step modulation method is illustrated in Fig. 7, as compared with the conventional one. The red arrow indicates the six active voltage vectors generated by the three-phase inverter, and the blue dotted line represents the division of the six-step modulation voltage sector. The voltage vector of the MI is divided into six sectors and the angle between the sectors is 60°. V_{active} is the active component of the reference voltage vector and it is parallel to the current vector I_S. As shown in Fig. 7(a), for the conventional six-step modulation

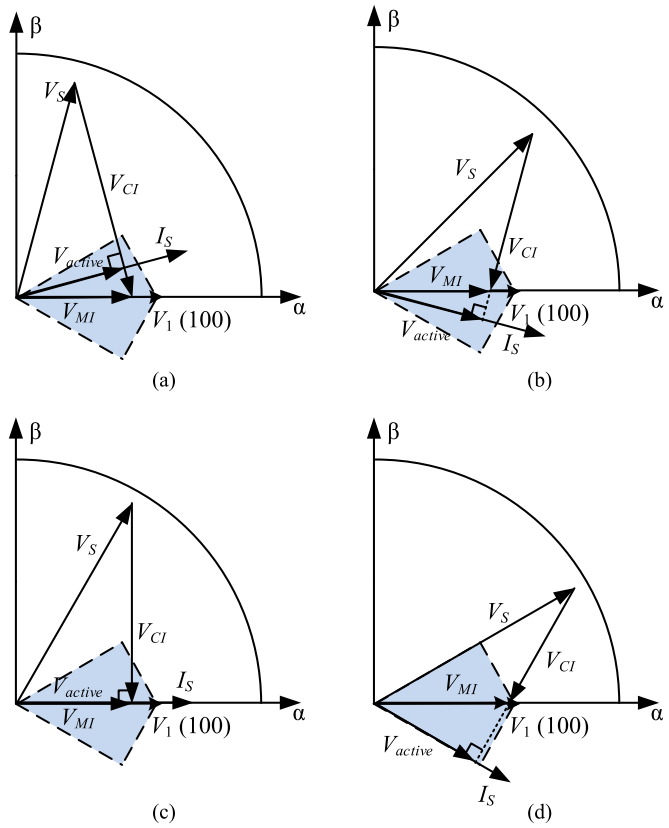

Fig. 8. Vector diagrams for different current angle in sector 1. (a) 15°. (b) −15°. (c) 0°. (d) −30°.

method, when the V_{active} locates in the angle range of $[-\pi/6, \pi/6)$, the voltage vector V_1 (1 0 0) is selected as the output voltage vector of the MI. Different from the conventional six-step modulation method, the improved six-step modulation consists of double vectors which contains one closest active voltage vector and one optimal zero voltage vector. For the improved six-step modulation method, in Fig. 7(b), when the V_{active} locates in the angle range of $[-\pi/6, \pi/6)$, the closest active voltage vector V_1 (1 0 0) and the zero voltage vector V_0 (0 0 0) are selected to synthesize the output voltage vector of the MI. By selecting the closest active voltage vector and the optimal zero voltage vector, V_{MI} can be accurately synthesized to satisfy the required active voltage of the motor. Compared with the conventional six-step modulation method, the improved six-step modulation method is applicable to the whole modulation range, so the switching frequency is reduced. In addition, the CI only needs to provide the reactive powers. Thus, the fluctuation of the capacitor voltage can also be reduced. The improved six-step modulation method is not only used in the health mode, but also can be in the fault-tolerant mode.

Figure 8 shows the vector diagrams of the improved six-step modulation according to the angle of current vector 15°, −15°, 0°, and −30° in sector 1. The outermost circle is the maximum modulation range. In sector 1, the closest active voltage vector V_1 (1 0 0) and the zero voltage vector V_0 (0 0 0) are selected to synthesize the output voltage vector of the MI, namely V_{MI}. In Fig. 8(a), when the angle of the current vector is 15°, the current vector I_S leads V_{MI}. The CI not only provides the reactive power required by the motor but also provides the reactive powers which output by the MI. When the angle of the current vector is −15°, the current vector I_S lags behind V_{MI}. The MI can supply a part of reactive powers. Therefore, the CI only supplies the rest of the reactive powers, as shown in Fig. 8(b). In Fig. 8(c), when the angle of the current vector is 0°, the current vector I_S is parallel to V_{MI}. The MI can only supply all the active powers required by the motor, while the CI can supply all the reactive powers. In Fig. 8(d), the angle of the current vector is −30° where is the edge of the sector 1, and the active voltage vector V_1 (1 0 0) and the zero voltage vector V_0 (0 0 0) are also selected to synthesize the output voltage vector of the MI.

TABLE I
DURATION OF VECTOR

sector	θ_i	V_X	V_Z	T_n
1	$[-\pi/6, \pi/6)$	V_1	V_0(000)	$3V_{\text{active}}Ts/2V_{\text{dc}}\cos(\theta_i)$
2	$[\pi/6, \pi/2)$	V_2	V_7(111)	$3V_{\text{active}}Ts/2V_{\text{dc}}\cos(\theta_i-\pi/3)$
3	$[\pi/2, 5\pi/6)$	V_3	V_0(000)	$3V_{\text{active}}Ts/2V_{\text{dc}}\cos(\theta_i-2\pi/3)$
4	$[5\pi/6, 7\pi/6)$	V_4	V_7(111)	$3V_{\text{active}}Ts/2V_{\text{dc}}\cos(\theta_i-\pi)$
5	$[7\pi/6, 3\pi/2)$	V_5	V_0(000)	$3V_{\text{active}}Ts/2V_{\text{dc}}\cos(\theta_i-4\pi/3)$
6	$[3\pi/2, 11\pi/6)$	V_6	V_7(111)	$3V_{\text{active}}Ts/2V_{\text{dc}}\cos(\theta_i-5\pi/3)$

As shown in Fig. 8, V_{active} is parallel to the current vector I_S. The amplitude of V_{active} and V_{MI} can be expressed as

$$\begin{cases} V_{\text{active}} = V_S\cos\varphi \\ V_{\text{MI}} = \frac{V_{\text{active}}}{\cos(\theta_{V_{\text{MI}}}-\theta_i)} \end{cases} \tag{10}$$

where $\theta_{V\,\text{MI}}$ is the angle of V_{MI}. In sector 1, the active vector V_1 (1 0 0) and the zero vector V_0 (0 0 0) is selected to synthesize V_{MI}, so under the volt–second balance principle, the relationship between V_{MI}, V_1, and V_0 can be calculated as

$$V_{\text{MI}}T_S = V_1T_n + V_0T_0 \tag{11}$$

where T_{s} is the switching period, T_n is the duration of V_1, T_0 is the duration of V_0, V_{dc} is the voltage of the dc link, and the amplitudes of the active vector V_1 and the zero vector V_0 are $2V_{\text{dc}}/3$ and 0.

Based on (10) and (11), the durations of the active vector V_1 and the zero vector V_0 can be obtained as

$$\begin{cases} T_n = \dfrac{3V_{\text{active}}}{2V_{\text{dc}}\cos(\theta_{V_{\text{MI}}}-\theta_i)}T_S \\ T_0 = T_S - T_n. \end{cases} \tag{12}$$

According to the foregoing analysis, when the current vector I_{s} lies in the other sectors, two vectors are selected and T_n is calculated as listed in Table I.

One of the advantages of the six-step modulation is its lower switching frequency, and the improved six-step modulation is also the same by selecting the optimal zero voltage vectors. In the improved six-step modulation method, when taking phase A as example, its switching state only changes in sector 1 and sector 4, while the switching state keeps high in sector 2 and sector 6 and keeps low in sector 3 and sector 5 without operation. Thus, the switching frequency of the improved six-step modulation is reduced to one-third of the conventional SVPWM. The switch-

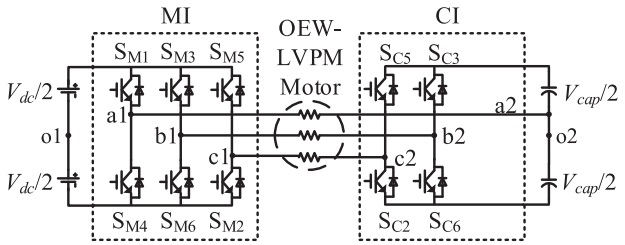

Fig. 9. Reconstructed topology of dual inverter under fault-tolerant condition.

ing loss is proportional to the switching frequency when the parameters of the system keep constant [27]. So, the switching loss in the improved six-step modulation is also reduced greatly.

By adopting the improved six-step modulation method, the MI can provide not only the active voltage required by the motor but also the reactive voltage with low switching frequency. Also, the CI only needs to supply the reactive power with a little fluctuation of capacitance voltage. It can be expressed as

$$\begin{cases} P_{\mathrm{MI}} = P_{\mathrm{OUT}} \\ Q_{\mathrm{CI}} + Q_{\mathrm{MI}} = Q_{\mathrm{OUT}}. \end{cases} \tag{13}$$

B. Fault-Tolerant Operation

As shown in Fig. 4, there are three SSRs. These SSRs connect the midpoint of each phase of the bridge arm to the neutral point of the capacitance, respectively. SSRs are all opened during healthy state. However, when a switch is broken in CI, the connection between the corresponding bridge arm and the capacitor is disconnected, and then the corresponding SSR is quickly closed. As a result, the corresponding phase winding is connected to the neutral point of the capacitors and the CI is restructured to three-phase four-switch topology. For example, when the switch S_{C1} is broken, the reconstructed topology is shown in Fig. 9.

Under open-circuit fault condition, the improved six-step modulation is still applied to the MI, and the fault-tolerant control strategy is activated in CI. Since only two-phase bridge arm can continue operation in the CI, only four active vectors are remained, namely 1′–4′. The switching states of the corresponding bridge arm are 0 0, 1 0, 1 1, 0 1, as depicted in Fig. 10. The red circle indicates the maximum modulation range which is the half of that at healthy operation. It can also be seen from Fig. 10 that no zero vector can be found. Therefore, the two inverse vectors need to act equal time in a switching period, such as voltage vectors 1′ and 4′. The proposed remedial method is suitable for other bridge arms with open-circuit fault.

Fig. 11 shows the space vector diagrams of the dual inverter in fault-tolerance state when capacitor voltage is doubled. There are total 32 space vector combinations. If the capacitor voltage is still in its original state V_{cap} ($V_{\mathrm{cap}} = V_{\mathrm{dc}}$), the maximum modulation range is 75% of that under the healthy condition. However, if the capacitor voltage is changed to $2V_{\mathrm{cap}}$, the maximum modulation range is the same as that in the healthy state. So the motor can operate as it is in the healthy state.

The control block diagram with the proposed hybrid modulation fault-tolerant control strategy is shown in Fig. 12. When a

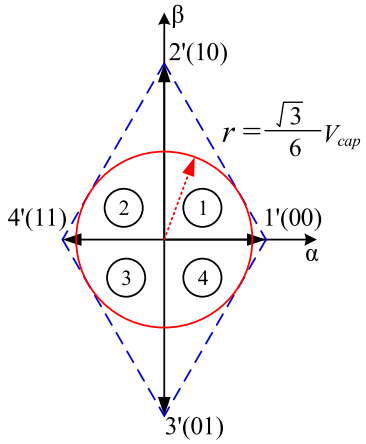

Fig. 10. Space vector distribution diagrams of CI.

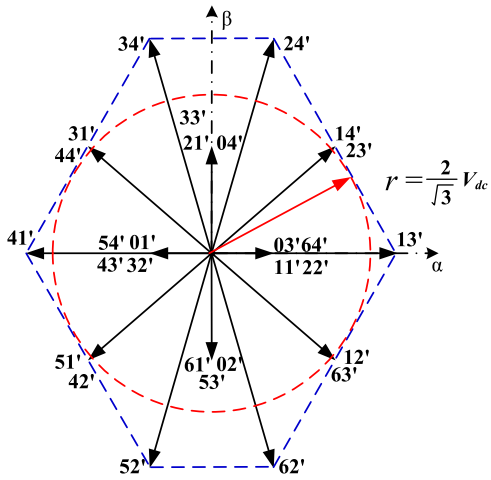

Fig. 11. Space vector diagrams of dual inverter under fault-tolerant condition.

switch is broken in CI, the CI is restructured to the three-phase four-switch topology. According to the above-analyzed hybrid fault-tolerant strategy, the reference vector is decoupled into two vectors (V_{MI} and V_{CI}). The outputs of current proportional-integral (PI) regulators transformed into active voltage vector V_{active} based on (10). Although the CI mainly provides reactive powers, it also needs to provide few active powers V_{CIactive} to compensate losses consumed by the inverter. So, the MI active voltage vector V_{MIactive} is composed of V_{active} and V_{CIactive}. Then, two different modulation methods are used in the MI and CI, separately. The improved six-step modulation is adopted in MI to synthetize V_{MI} and the fault-tolerant control strategy is activated in CI to synthetize V_{CI}.

IV. Simulation

To verify the proposed hybrid modulation fault-tolerant control strategy, simulations in a MATLAB/Simulink environment are performed. When one switch is with open-circuit fault, the CI is restructured to the three-phase four-switch topology in Fig. 9. The simulations are performed under this open-circuit

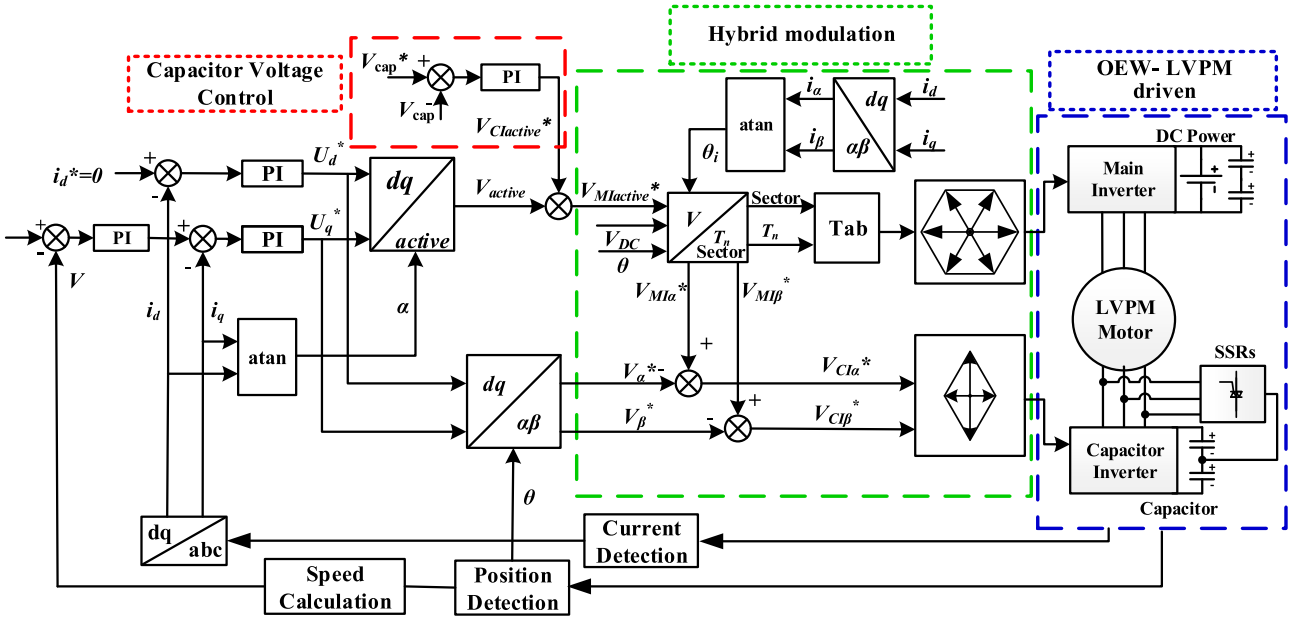

Fig. 12. Control block diagram with proposed hybrid modulation fault-tolerant control strategy.

TABLE II
LVPM MOTOR PARAMETERS

Parameters	Symbol	Value
Stator resistance (Ω)	R_s	1.12
d-axis inductance (mH)	L_d	84.8
q-axis inductance (mH)	L_q	86
Permanent flux linkage (Wb)	ψ_{PM}	0.105
Pole pitch (m)	τ_s	0.0147
Mover weight (kg)	M	32
Number of the poles	n_p	2

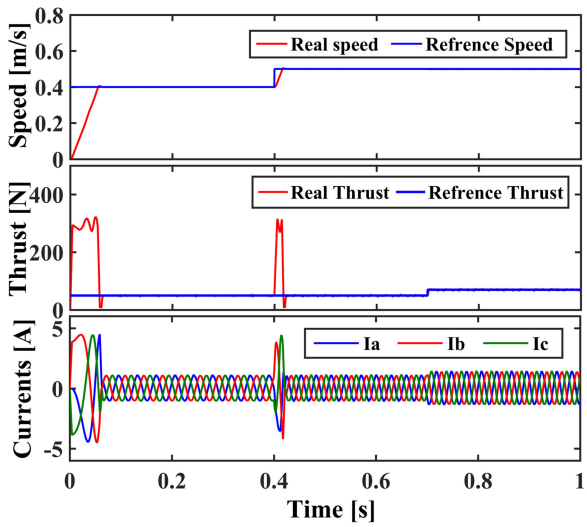

Fig. 13. Speed, thrust, and currents performance at the proposed fault-tolerant operation.

fault condition. The simulation results are shown in this section. The parameters of the OEW-LVPM motor are given in Table II.

Figure 13 shows the speed, thrust, and currents performance at the proposed fault-tolerant operation. At the time 0.4 s, a step change in command velocity occurs from 0.4 to 0.5 m/s; at the time 0.7 s, a step change in thrust occurs from 70 to 90 N. With the change of the reference speed and reference thrust, the frequency and amplitude of a three-phase currents also change. Obviously, the proposed fault-tolerant strategy has good dynamic and steady-state performance under different operating condition.

Figure 14 compares the MI sector and switch state in healthy and fault-tolerant modes. In this paper, the open-circuit fault occurs in the CI. The improved six-step modulation used in the MI is the same at pre-/postfault, so the MI sector and the switch state are also the same. It can be seen that the switch operates only on sector 1 and sector 4. The switching frequency of the conventional SVPWM modulation is usually 10 kHz. However, the switching frequency of the improved six-step modulation is about 3.4 kHz. Thus, the switching frequency is reduced by about 2/3. Since the switching loss is in proportion to the switching frequency when other parameters stay constant, the switching loss is also reduced.

The stability of a capacitor voltage is an important issue of the whole control system. In this study, a voltage controller is designed by PI controller to balance the capacitor voltage in constant. From Fig. 15, the capacitor voltage can be balanced in a stable level. Digital filters with same cut-off frequency are used to extract the fundamental wave of capacitor voltage, as well as the phase-current. In order to show more clearly, the current is ten times larger. It can be seen that the capacitor voltage lags behind the current 90° to compensate all of the reactive components. Under fault-tolerant condition, the CI runs in only four sectors.

V. EXPERIMENT RESULTS

In order to verify the proposed control strategy, a test platform has been set up, as shown in Fig. 16. The timing calculations,

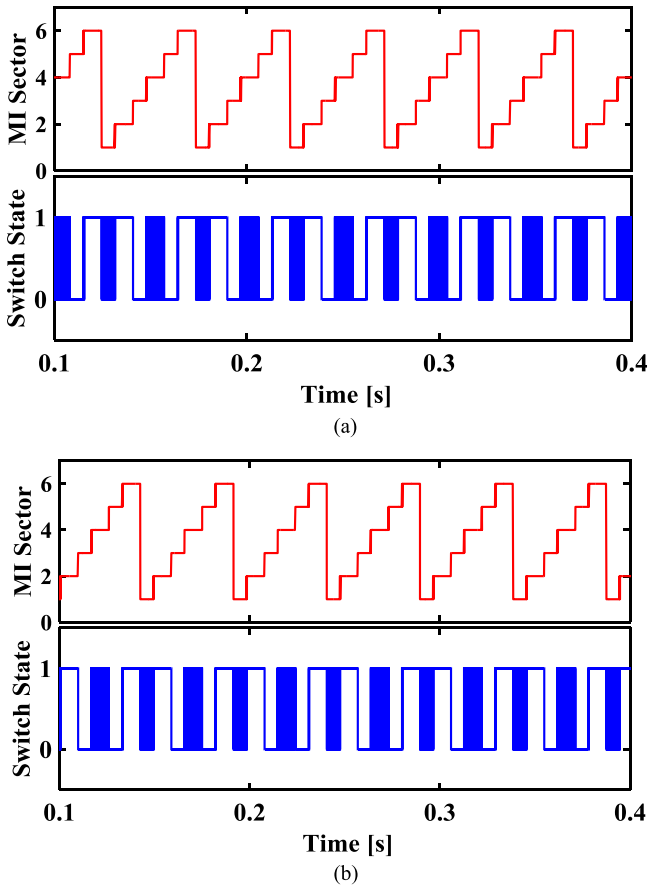

Fig. 14. Comparison of MI sector and switch state in healthy and fault-tolerant modes. (a) Healthy mode. (b) Fault-tolerant mode.

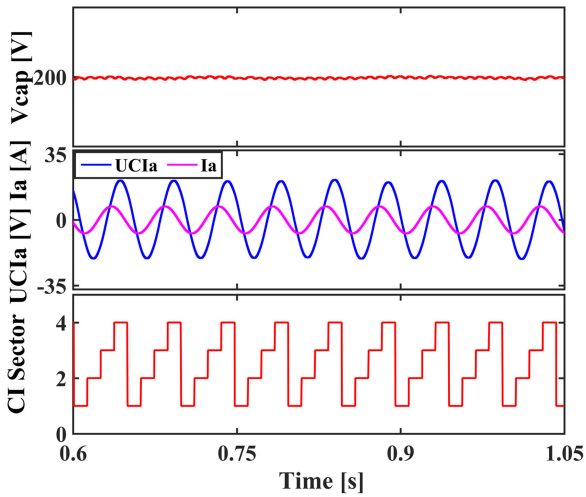

Fig. 15. Top to bottom: Capacitor voltage, the relationship between phase voltage and phase current, CI sector at the proposed fault-tolerant operation.

voltage controllers, PWM signal generation, and the control scheme are implemented on TMS320F2812 DSP. Two intelligent power modules PM100CVA120 are used. The dc-link voltage of MI is 80 V and the capacitor of CI is 160 V. Thus, under the fault-tolerant condition, the motor can achieve the same

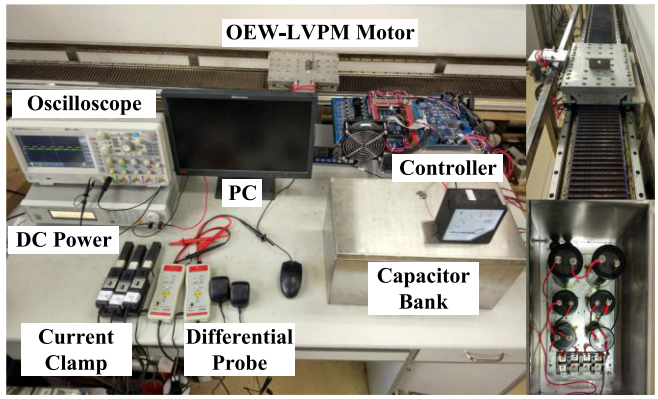

Fig. 16. Experimental platform.

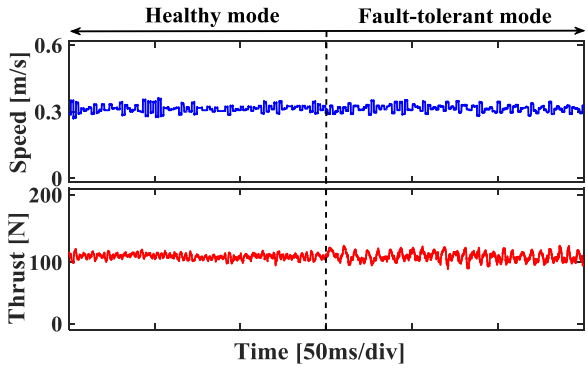

Fig. 17. Comparison of speed and thrust in healthy and fault-tolerant modes.

state as it is in the healthy condition. Two capacitors (4700 μF) are chosen to supply all the reactive powers.

Figure 17 compares the speed and thrust performances in the healthy and fault-tolerant modes. By using the proposed fault-tolerant control strategy, at the speed of 0.3 m/s, the motor can all run steadily.

The control strategy used in the MI always remains unchanged under any condition. So, for the MI, its sector and switch state also should be same. From Fig. 18, it can be seen that no distortion occur in the three-phase current before and after the fault. The MI sector and switch state of one phase are shown in second and third figure, respectively. The switch operates only on sector 1 and sector 4, and the switching frequency is reduced.

Figure 19 shows the experimental waveforms of the capacitor voltage and the CI sector. Before and after the fault, by using the proposed fault-tolerant control strategy, the capacitor voltage keeps steady at 160 V. Thus, the CI can supply all the reactive power. For the CI sector, by reconstructing the CI to the three-phase four-switch topology, the number of the CI sector is reduced to 4. It can be known from the bottom figure.

Figure 20 reflects the relationship between the filtered voltage in the CI and the currents at stepped load. It can be seen that the rise of the current amplitude corresponds to the up-loading process. The phase current leads phase voltage of 90°, so the CI only supplies the reactive powers.

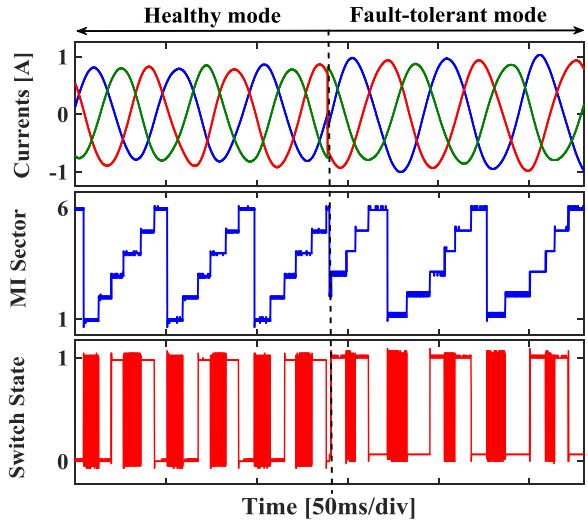

Fig. 18. Comparison of three-phase currents, MI sector, and switch state in healthy and fault-tolerant modes.

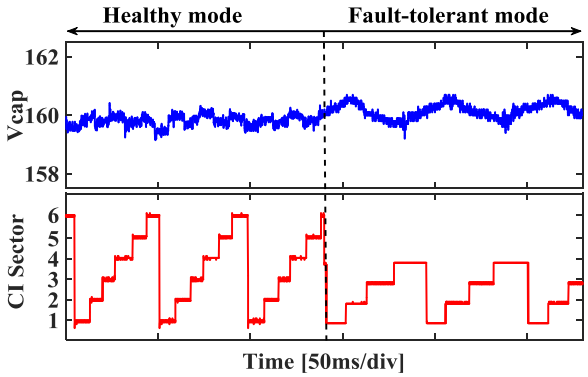

Fig. 19. Comparison of capacitor voltage and CI sector in healthy and fault-tolerant modes.

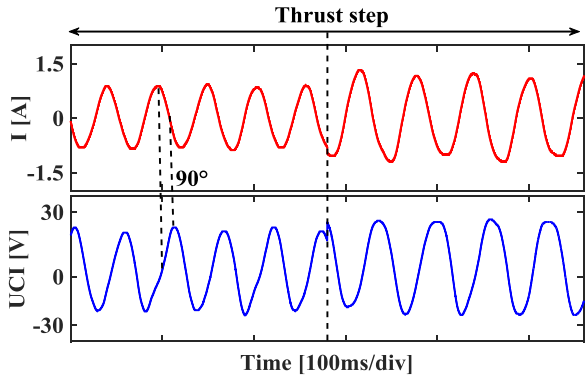

Fig. 20. Relationship between filtered phase voltage and phase current in load stepped.

Figure 21 shows the speed performance at the proposed fault-tolerant operation. At the time 1.5 s, a step change in command velocity occurs from 0.25 to 0.35 m/s; obviously, the proposed fault-tolerant strategy has a good dynamic performance.

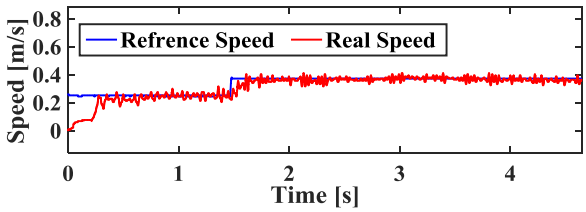

Fig. 21. Speed performance at the proposed fault-tolerant operation.

VI. Conclusion

This paper has proposed a hybrid modulation fault-tolerant control strategy for the OEW-LVPM motor with a floating CI, which can improve the fault-tolerant ability when one certain switch in CI is broken. Under the open-circuit fault condition, the improved six-step modulation is used in the MI, and the fault-tolerant control strategy is activated in CI. The improved six-step modulation consists of double vectors, which contains one closest active voltage vector and one optimal zero voltage vectors. Thus, the MI can provide all the active powers with lower switching frequency as well as switching loss. By reconstructing the CI to the three-phase four-switch topology, CI only needs to compensate the reactive power with less capacitor voltage ripple. A voltage controller is also designed by the PI controller to keep the capacitor voltage invariable. So, the OEW-LVPM system efficiency is enhanced. The motor can keep operation as prefault. The simulation and experimental studies have proven that the proposed fault-tolerant control strategy has a good performance.

References

[1] G. Lv, T. Zhou, D. Zeng, and Z. Liu, "Design of ladder-slit secondaries and performance improvement of linear induction motors for urban rail transit," *IEEE Trans. Ind. Electron.*, vol. 65, no. 2, pp. 1187–1195, Feb. 2018.

[2] W. Zhao, B. Wu, Q. Chen, and J. Zhu, "Fault-tolerant direct thrust force control for a dual inverter fed open-end winding linear vernier permanent-magnet motor using improved SVPWM," *IEEE Trans. Ind. Electron.*, vol. 65, no. 9, pp. 7458–7467, Sep. 2018.

[3] G. Lv, D. Zeng, T. Zhou, and Z. Liu, "Investigation of forces and secondary losses in linear induction motor with the solid and laminated back iron secondary for metro," *IEEE Trans. Ind. Electron.*, vol. 64, no. 6, pp. 4382–4390, Jun. 2017.

[4] D. Hu, W. Xu, R. Dian, Y. Liu, and J. Zhu, "Loss minimization control of linear induction motor drive for linear metros," *IEEE Trans. Ind. Electron.*, vol. 65, no. 9, pp. 6870–6880, Sep. 2018.

[5] G. Pellegrino, A. Vagati, B. Boazzo, and P. Guglielmi, "Comparison of induction and PM synchronous motor drives for EV application including design examples," *IEEE Trans. Ind. Appl.*, vol. 48, no. 6, pp. 2322–2332, Nov./Dec. 2012.

[6] W. Zhao, J. Zheng, J. Wang, G. Liu, J. Zhao, and Z. Fang, "Design and analysis of a linear permanent-magnet vernier machine with improved force density," *IEEE Trans. Ind. Electron.*, vol. 63, no. 4, pp. 2072–2082, Apr. 2016.

[7] G. H. B. Foo and X. Zhang, "Robust direct torque control of synchronous reluctance motor drives in the field-weakening region," *IEEE Trans. Power Electron.*, vol. 32, no. 2, pp. 1289–1298, Feb. 2017.

[8] S. K. Sahoo and T. Bhattacharya, "Field weakening strategy for a vector-controlled induction motor drive near the six-step mode of operation," *IEEE Trans. Power Electron.*, vol. 31, no. 4, pp. 3043–3051, Apr. 2016.

[9] S. Du and B. Wu, "A transformerless bipolar modular multilevel DC-DC converter with wide voltage ratios," *IEEE Trans. Power Electron.*, vol. 32, no. 11, pp. 8312–8321, Nov. 2017.

[10] M. Forouzesh, Y. P. Siwakoti, S. A. Gorji, F. Blaabjerg, and B. Lehman, "Step-up DC-DC converters: A comprehensive review of voltage-boosting techniques, topologies, and applications," *IEEE Trans. Power Electron.*, vol. 32, no. 12, pp. 9143–9178, Dec. 2017.
[11] Q. An, J. Liu, Z. Peng, L. Sun, and L. Sun, "Dual-space vector control of open-end winding permanent magnet synchronous motor drive fed by dual inverter," *IEEE Trans. Power Electron.*, vol. 31, no. 12, pp. 8329–8342, Dec. 2016.
[12] D. Wu, X. Wu, L. Su, X. Yuan, and J. Xu, "A dual three-level inverter-based open-end winding induction motor drive with averaged zero-sequence voltage elimination and neutral-point voltage balance," *IEEE Trans. Ind. Electron.*, vol. 63, no. 8, pp. 4783–4795, Aug. 2016.
[13] Y. Zhou and H. Nian, "Zero-sequence current suppression strategy of open-winding PMSG system with common DC bus based on zero vector redistribution," *IEEE Trans. Ind. Electron.*, vol. 62, no. 6, pp. 3399–3408, Jun. 2015.
[14] V. T. Somasekhar, S. Srinivas, and K. K. Kumar, "Effect of zero-vector placement in a dual-inverter fed open-end winding induction-motor drive with a decoupled space-vector PWM strategy," *IEEE Trans. Ind. Electron.*, vol. 55, no. 6, pp. 2497–2505, Jun. 2008.
[15] V. T. Somasekhar, B. Venugopal Reddy, and K. Sivakumar, "A four-level inversion scheme for a 6n-pole open-end winding induction motor drive for an improved DC-link utilization," *IEEE Trans. Ind. Electron.*, vol. 61, no. 9, pp. 4565–4572, Sep. 2014.
[16] S. Lakhimsetty, N. Surulivel, and V. T. Somasekhar, "Improvised SVPWM strategies for an enhanced performance for a four-level open-end winding induction motor drive," *IEEE Trans. Ind. Electron.*, vol. 64, no. 4, pp. 2750–2759, Apr. 2017.
[17] J. Hong, H. Lee, and K. Nam, "Charging method for the secondary battery in dual-inverter drive systems for electric vehicles," *IEEE Trans. Ind. Electron.*, vol. 30, no. 2, pp. 909–921, Mar. 2014.
[18] S. Pramanick, N. A. Azeez, R. S. Kaarthik, K. Gopakumar, and C. Cecati, "Low-order harmonic suppression for open-end winding IM with dodecagonal space vector using a single DC-link supply," *IEEE Trans. Ind. Electron.*, vol. 62, no. 9, pp. 5340–5347, Sep. 2015.
[19] S. Pramanick, M. Boby, N. A. Azeez, K. Gopakumar, and S. S. Williamson, "A three-level dodecagonal space vector-based harmonic suppression scheme for open-end winding IM drives with single-DC supply," *IEEE Trans. Ind. Electron.*, vol. 63, no. 11, pp. 7226–7233, Nov. 2016.
[20] S. Chowdhury, P. W. Wheeler, C. Patel, and C. Gerada, "A multilevel converter with a floating bridge for open-end winding motor drive applications," *IEEE Trans. Ind. Electron.*, vol. 63, no. 9, pp. 5366–5375, Sep. 2016.
[21] Y. Lee and J. I. Ha, "Hybrid modulation of dual inverter for open-end permanent magnet synchronous motor," *IEEE Trans. Power Electron.*, vol. 30, no. 6, pp. 3286–3299, Jun. 2015.
[22] D. Pan, F. Liang, Y. Wang, and T. A. Lipo, "Extension of the operating region of an IPM motor utilizing series compensation," *IEEE Trans. Ind. Appl.*, vol. 50, no. 1, pp. 539–548, Jan./Feb. 2014.
[23] J. Kim, J. Jung, and K. Nam, "Dual-inverter control strategy for high-speed operation of EV induction motors," *IEEE Trans. Ind. Electron.*, vol. 51, no. 2, pp. 312–320, Apr. 2004.
[24] N. K. Nguyen, F. Meinguet, E. Semail, and X. Kestelyn, "Fault-tolerant operation of an open-end winding five-phase PMSM drive with short-circuit inverter fault," *IEEE Trans. Ind. Electron.*, vol. 63, no. 1, pp. 595–605, Jan. 2016.
[25] J. He *et al.*, "A fast on-line diagnostic method for open-circuit switch faults in SiC-MOSFET-based-type multilevel inverters," *IEEE Trans. Ind. Appl.*, vol. 53, no. 3, pp. 2948–2958, May/Jun. 2017.
[26] L. M. A. Caseiro and A. M. S. Mendes, "Real-time IGBT open-circuit fault diagnosis in three-level neutral-point-clamped voltage-source rectifiers based on instant voltage error," *IEEE Trans. Ind. Electron.*, vol. 62, no. 3, pp. 1669–1678, Mar. 2015.
[27] Y. Wu, M. A. Shafi, A. M. Knight, and R. A. McMahon, "Comparison of the effects of continuous and discontinuous PWM schemes on power losses of voltage-sourced inverters for induction motor drives," *IEEE Trans. Power Electron.*, vol. 26, no. 1, pp. 182–191, Jan. 2011.

Wenxiang Zhao (M'08–SM'14) received the B.Sc. and M.Sc. degrees in electrical engineering from Jiangsu University, Zhenjiang, China, in 1999 and 2003, respectively, and the Ph.D. degree in electrical engineering from Southeast University, Nanjing, China, in 2010.

From 2008 to 2009, he was a Research Assistant with the Department of Electrical and Electronic Engineering, University of Hong Kong, Hong Kong. From 2013 to 2014, he was a Visiting Professor with the Department of Electronic and Electrical Engineering, University of Sheffield, Sheffield, U.K. Since 2003, he has been with Jiangsu University, where he is currently a Professor with the School of Electrical Information Engineering. His current research interests include electric machine design, modeling, fault analysis, and intelligent control. He has authored and coauthored more than 200 technical papers in these areas.

Peng Zhao received the B.Sc. degree in electrical engineering from Jiangsu University, Zhenjiang, China, in 2016, where he is currently working toward the M.Sc. degree in electrical engineering.

His research interest focuses on the control of permanent-magnet machines.

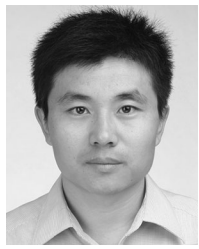

Dezhi Xu received the B.Sc. degree in electrical engineering from Hebei University of Science and Technology, Shijiazhuang, China, in 2003, the M.Sc. degree in electrical engineering from Guizhou University, Guiyang, China, in 2006, and the Ph.D. degree in electrical engineering from Shanghai University, Shanghai, China, in 2015.

Since 2015, he has been with Jiangsu University, Zhenjiang, China, where he is currently a Lecturer with the School of Electrical and Information Engineering. His current research interests include topologies, PWM techniques, and fault-tolerant control of multilevel and multiphase permanent-magnet synchronous machine drive systems.

Zhonghua Chen received the B.Sc. degree in electrical engineering from Jiangsu University, Zhenjiang, China, in 2015, where he is currently working toward the M.Sc. degree in electrical engineering.

His research interests include motor drive and control of permanent-magnet motors.

Jihong Zhu received the B.Sc. degree in electrical engineering from Jiangsu University, Zhenjiang, China, in 1990, and the Ph.D. degree in control engineering from Nanjing University of Science and Technology, Nanjing, China, in 1995.

From 1996 to 1997, he was with Nanjing University of Aeronautics and Astronautics, Nanjing, where was a Postdoctoral Fellow and Associate Professor, respectively. Since 1998, he has been with Tsinghua University, Beijing, China, where he is currently a Professor. His teaching and research interests include motor control and flight control. He has authored or coauthored more than 150 technical papers, and is the holder of more than 60 patents in these areas.